AAS 24-368

RESONANCE WIDTHS, CHAOTIC ZONES, AND TRANSPORT IN CISLUNAR SPACE

Anjali Rawat[*], Bhanu Kumar[†], Aaron J. Rosengren[‡], and Shane D. Ross[§]

Lunar mean-motion resonances (MMRs) significantly shape cislunar dynamics beyond GEO forming stable-unstable pairs, with corresponding intermingled chaotic and regular regions. The resonance zone is rigorously defined using the separatrix of unstable resonant periodic orbits surrounding stable quasi-periodic regions. Our study leverages the restricted three-body problem to estimate the (stable) resonance widths and (unstable) chaotic resonance zones of influence of the 2:1 and 3:1 MMRs across various Jacobi constants, employing a Poincaré map at perigee and presenting findings in easily interpretable geocentric orbital elements. An analysis of the semi-major axis versus eccentricity plane reveals broader regions of resonance influence than those predicted by semi-analytical models based on the perturbed Kepler problem. A comparison with observed spacecraft in these regions is made, showing excellent agreement.

I. INTRODUCTION

The dynamics of cislunar space beyond GEO (xGEO) are fundamentally influenced by mean-motion resonances (MMRs), a factor previously underappreciated due to their negligible effect on low-Earth orbit satellites. However, for missions like IBEX and TESS, operating within predominant lunar MMRs, and others like Spektr-R, which seemingly navigates unstable resonance regions, recognizing the impacts of MMRs is crucial. Determining the stability of a space asset's xGEO orbit necessitates a thorough understanding of the dynamical structure of MMRs, particularly the extent of stable MMRs and the surrounding chaotic regions across various semi-major axis values.

Various semi-analytical methods, such as Gallardo's algorithm,[1] have been used to assess the domain of influence of predominant MMRs. Yet, these methods often presuppose constant eccentricity over resonant timescales, which does not accurately reflect the highly perturbed Earth-Moon environment of xGEO. Such approaches, moreover, are fundamentally based on the perturbed-Hamiltonian formulation, which provides a local, rather than global, picture of specific regions of phase space. A global geometric dynamical portrait can be furnished by semi-analytical approaches to the circular, restricted, three-body problem (CR3BP). While some methods integrate the full CR3BP model, they do not utilize Delaunay variables — which offer analytical benefits for revealing Hamiltonian structure — in favor of alternative variables for Poincaré maps.[2] Consequently, such methods tend to underestimate MMR widths and neglect the presence of unstable periodic resonant orbits, critical for understanding transit through large connected chaotic zones that dominate at small values of the Jacobi constant.

[*]PhD Student, Aerospace and Ocean Engineering, Virginia Tech, Blacksburg, VA, United States, anjalirawat@vt.edu
[†]NSF Postdoctoral Research Fellow, Jet Propulsion Laboratory, California Institute of Technology, Pasadena, CA, United States, Current Email: bkumar@mathi.uni-heidelberg.de
[‡]Assistant Professor, Mechanical and Aerospace Engineering, University of California San Diego, La Jolla, CA, United States, arosengren@ucsd.edu
[§]Professor, Aerospace and Ocean Engineering, Virginia Tech, Blacksburg, VA, United States, sdross@vt.edu

This study computes the semi-major axis *stable resonance widths* and the larger circumscribing *unstable resonance zones* of influence for key lunar MMRs, specifically the 2:1 and 3:1 resonances, using the planar CR3BP, following known methods.[3–7] By applying a Poincaré map at the perigee of osculating orbits,[5,7] we delineate these regions in terms of the semi-major axis versus the argument of perigee relative to the Earth-Moon line (the *synodic* perigee). Our Poincaré maps reveal resonance regions, notably the prominent 2:1, 3:1, and 4:1 resonance 'islands', through which we can determine the *stable* width of a resonance, defined as the semi-major axis span of the 'largest' (i.e., outermost) stable quasi-periodic torus. Unstable resonant periodic orbits are computed via symmetry, and their stable and unstable manifolds are visualized on the Poincaré map. Chaotic (resonance) zones are identified as regions enclosed by the boundaries identified as the union of segments of stable and unstable manifolds, according to well-established dynamical-systems methods.[8,9] Resonance widths and the larger enclosing chaotic resonance zones are computed across a range of Jacobi constants, subsequently correlating the widths with projections of PCR3BP energy surfaces onto the osculating eccentricity (e) versus semi-major axis (a) plane. The directly computed PCR3BP-based stable resonance zone widths are compared with semi-analytical predictions.[1,10,11] Moreover, the orbits of both historic and current xGEO spacecraft, obtained via their two-line element (TLE) sets, are projected onto the (a, e)-plane to ascertain their positioning within stable or unstable resonance regions.

This paper is structured into ten sections. Section I introduces the problem's motivation and reviews relevant prior research. Section II provides a concise overview of the CR3BP. Section III details key aspects of Poincaré maps, focusing on stable and unstable periodic orbits, and defining stable resonance widths and the larger chaotic resonance regions. Section IV explores MMRs in xGEO, highlighting both stable and unstable periodic orbits. Section V outlines the methodology for identifying unstable fixed points and their stable and unstable manifolds. Section VI presents summarized findings from a semi-analytical approach assessing MMR widths. Section VII discusses the methodology employed to determine resonance widths and chaotic zones, mapping them onto the (a, e) plane, and compares with semi-analytically computed widths and TLEs of spacecraft. Section VIII explores potential heteroclinic transfers, including transfer timings. Section IX provides a discussion on the interaction of the L1 Lyapunov orbit manifold tubes with MMR manifolds. Finally, Section X provides a summary of the paper's results and future works.

II. PLANAR, CIRCULAR, RESTRICTED, THREE-BODY PROBLEM

The planar CR3BP (PCR3BP for short) is the simplest model for motion in cislunar space whose dynamics capture the main qualitative features of the true motion. It describes the motion of a massless spacecraft relative to two primary bodies (e.g., Earth and Moon), viewed in a rotating frame centered at the center of mass (barycenter) of the two primaries. The PCR3BP assumes the motion of both primaries move in circular orbits with constant angular velocity about their barycenter, and all three bodies move in a single plane.

In the equations of motion of the PCR3BP we choose normalized units such that the distance (a_m) between the two masses m_1 and m_2 is 1, their combined mass is 1, and the period of their orbit relative to the barycentered inertial frame, i.e., the sidereal period T_m, is 2π. The only parameter of the system dynamics is then the mass ratio μ, defined as $\frac{m_2}{m_1+m_2}$. For the Earth-Moon system, we use $\mu = 1.2150584270571545 \times 10^{-2}$. We choose a coordinate frame rotating, as in Figure 1(a), with the two massive bodies and centered at their barycenter with m_1 and m_2 lying on the x-axis at $(-\mu, 0)$ and $(1-\mu, 0)$, respectively. The PCR3BP second-order differential equations of motion for the spacecraft in the normalized units is then,

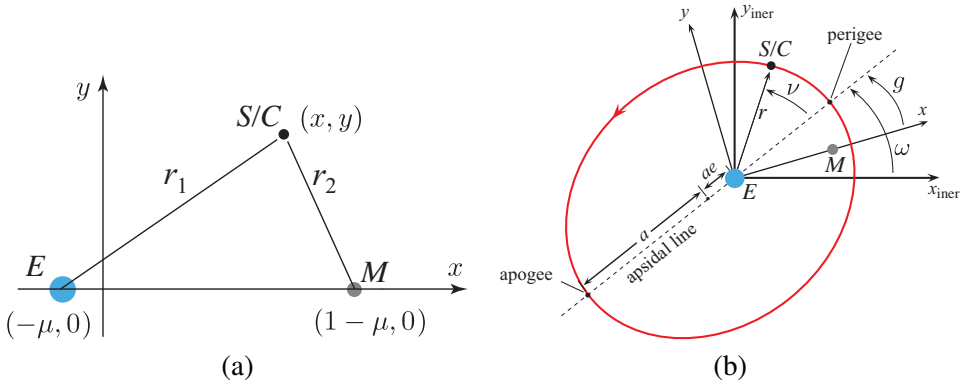

Figure 1: (a) The planar circular restricted three-body problem (PCR3BP) geometry in the non-dimensional co-rotating (x, y) frame models the motion of a spacecraft S/C with respect to the Earth (E) and Moon (M). (b) The osculating or instantaneous orbital elements for a spacecraft in a geocentric orbit about the Earth. The argument of perigee with respect to an inertial frame (ω) and the rotating frame (g) are shown, as is the true anomaly (ν).

$$\begin{aligned} \ddot{x} - 2\dot{y} &= x - (1-\mu)\frac{x+\mu}{r_1^3} - \mu\frac{x-1+\mu}{r_2^3}, \\ \ddot{y} + 2\dot{x} &= y - (1-\mu)\frac{y}{r_1^3} - \mu\frac{y}{r_2^3}, \end{aligned} \tag{1}$$

where $r_1 = \sqrt{(x+\mu)^2 + y^2}$ is the distance from the spacecraft to the primary body and $r_2 = \sqrt{(x-1+\mu)^2 + y^2}$ is the distance to the secondary. In general, we refer to a point in the 4-dimensional phase-space manifold $\mathcal{M}$ as X. This point can be written in terms of the rotating frame Cartesian coordinates given above, $X = (x, y, \dot{x}, \dot{y})$. Alternatively, in the geocentric part of $\mathcal{M}$, one can use instantaneous (i.e., osculating) geocentric orbital elements, e.g., $X = (a, e, \ell, g)$, where a is the semi-major axis, e the eccentricity, ℓ the mean anomaly, and g the perigee angle with respect to the positive x-axis, as depicted in Figure 1(b).

Jacobi Constant and the Energy Manifold. The Jacobi constant is proportional to the negative of the Hamiltonian energy of the system and is a constant of motion of the CR3BP equations. In other words, for an initial condition $X \in \mathcal{M}$, this scalar value does not change. The formula we use for the Jacobi constant is, *

$$\mathcal{C}(x, y, \dot{x}, \dot{y}) = x^2 + y^2 + 2\left(\frac{1-\mu}{r_1} + \frac{\mu}{r_2}\right) - \left(\dot{x}^2 + \dot{y}^2\right). \tag{2}$$

Let $\mathcal{M}_C$ be the energy manifold or energy surface given by setting the Jacobi integral (2) equal to a constant, i.e.,

$$\mathcal{M}_C = \{X \in \mathcal{M} \mid \mathcal{C}(X) = C = \text{constant}\}. \tag{3}$$

The surface $\mathcal{M}_C$ can be considered as a 3-dimensional manifold embedded in the 4-dimensional phase space $\mathcal{M}$. For the geocentric portion of $\mathcal{M}_C$ interior to the Moon's orbit, dimensionality can be further reduced by using a 2-dimensional Poincaré surface of section, described in section III.

*We note that this definition differs from some authors, who add a constant value $\mu(1-\mu)$, so that the Jacobi constant of the L_4, L_5 points is precisely 3. We adopt the convention in current use among the cislunar astrodynamics community.

Tisserand Parameter. An approximation to the Jacobi constant in orbital-element space with respect to the Moon is the Tisserand parameter ($T \approx C$), defined in the PCR3BP as,

$$T = \frac{1}{a} + 2\sqrt{a(1-e^2)}, \tag{4}$$

which dynamically limits the range of motion a non-maneuvering spacecraft is capable of, depicted using the geocentric orbital elements semi-major axis (a) and eccentricity (e).

III. THE POINCARÉ MAP AND KEY DYNAMICAL FEATURES

Surface of Section at Perigee

In our study, we define the Poincaré surface of section at perigee crossings identified when the geocentric mean anomaly ℓ is zero (same condition as true anomaly ν equals zero). We introduce a function,

$$h(\ell) = \cos\ell + \tfrac{1}{4}\sin\ell - 1, \tag{5}$$

which only crosses zero in an increasing direction when $\ell = 0$ (perigee), effectively preventing false detections of perigee during apogee where $\ell = \pi$.* Therefore our Poincaré section, parametrized by Jacobi constant C, is defined as,

$$\Sigma_C = \{X \in \mathcal{M}_C \mid h(\ell) = 0\}. \tag{6}$$

The Poincaré section so constructed can be represented by two variables that can be interpreted in orbital-element variables: the semi-major axis a and the synodic argument of perigee g, the angle between perigee and the Moon's location in the rotating frame, Figure 1. As g is an angular variable, Σ_C has a cylindrical topology, i.e., $(a, g) \in I \times S^1$ where $I \subset \mathbb{R}$, and S^1 is the circle.

Poincaré Map on the Poincaré Section

Poincaré maps simplify the study of the PCR3BP by transforming a four-dimensional phase space into a more manageable two-dimensional analysis, elucidating periodic, quasi-periodic, and chaotic

*If the spacecraft near apoapsis, $\ell = \pi$, comes close to the Moon, then the mean anomaly ℓ can momentarily decrease. If one uses an events function that, as ℓ increases, crosses zero at perigee and apogee in increasing and decreasing directions respectively, this momentary decrease in ℓ can trigger a false detection of $\ell = 0$ even when in reality the spacecraft is going through $\ell = \pi$. The above h crosses zero at $\ell = 0$ and $\ell \approx 0.49$ rad in increasing/decreasing directions, respectively; at the latter point the spacecraft is not influenced strongly enough by the Moon for ℓ to start decreasing, so the issue is avoided.

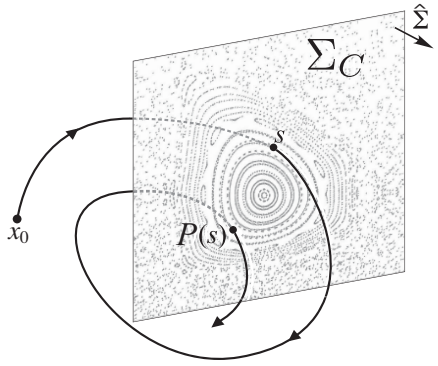

Figure 2: Poincaré map P on the Poincaré section Σ_C in the PCR3BP. The unit vector $\hat{\Sigma}$ gives the sense in which trajectories are crossing Σ_C.

behaviors, and revealing the intricate manifold structures that govern the system's dynamics. Let Σ_C represent a 2-dimensional surface transverse to the flow along the energy manifold $\mathcal{M}_C$, (Figure 2), and let x_0 denote an initial state, not necessarily in Σ_C. The Poincaré map $P(x_0) = s$ corresponds to the first crossing of Σ_C by the trajectory originating at x_0 in a particular direction. In general, we will consider mappings of Σ_C to itself,

$$\begin{aligned} P : \Sigma_C &\to \Sigma_C, \\ s &\mapsto P(s). \end{aligned} \tag{7}$$

We establish important terminology below.

Definition 1. *The "orbit" of a point $s \in \Sigma_C$ under P is the set of all the past and future iterates of the point s under the map P, i.e., the infinite sequence of points, $\{\ldots, P^{-1}(s), s, P^1(s), P^2(s), \ldots\}$, also denoted as $\mathcal{O}(s)$. See Figures 2 and 3(a) for examples of points and their iterates under the map P. Note that the orbit of s is the same as the orbit of $P^k(s)$ for all $k \in \mathbb{Z}$, and all represent the same continuous "trajectory" within the energy manifold $\mathcal{M}_C$.*

Some orbits of P do not contain an infinite number of distinct points, but instead have a finite number of distinct points. These are periodic orbits of P in the sense that the sequence repeats after some minimum integer $n \geq 1$ number of iterates.

Definition 2. *A periodic orbit of P is a finite sequence of points $\mathcal{O}(p_n) = \{p_1, \ldots, p_n\}$ such that $p_k = P(p_{k-1})$ for $2 \leq k \leq n$ and $p_1 = P(p_n)$. The period-n points $\mathcal{O}(p_n)$ represent a continuous periodic trajectory, a closed loop, within the energy manifold $\mathcal{M}_C$.*

This is a generalization of fixed points, as the state returns to the initial point $p_1 \in \Sigma$ after n iterates of the Poincaré map, i.e., $p_1 = P^n(p_1)$, where P^n denotes n compositions of P, $P \circ P \circ \cdots \circ P \circ P$ (n times). For a periodic orbit, we note that each of the points $p_1, \ldots, p_n$ is a fixed point (a period-1 point) under n iterates of the map, i.e., $p_k = \bar{P}(p_k)$, where $\bar{P} = P^n$, and thus we may occasionally refer to each one individually as a fixed point.

If a periodic orbit $\mathcal{O}(p_n)$ is of saddle-type, each of the points $p_1, \ldots, p_n \in \mathcal{O}(p_n)$ will have stable ($W^s(p_i)$) and unstable ($W^u(p_i)$) invariant manifolds, for $i = 1, \ldots, n$, consisting of orbits of P which tend asymptotically toward and away from $\mathcal{O}(p_n)$, respectively. It is known that for two-dimensional maps from 2 degree-of-freedom Hamiltonian systems,[12,13] some periodic orbits $\mathcal{O}(p_n)$ are related to a general idea of "resonance", beyond just the application to orbital dynamics. If $\mathcal{O}(p_n)$ is of center-type stability, this is a stable resonant orbit. If $\mathcal{O}(p_n)$ is of saddle-type stability, this is an unstable resonant orbit. It should be noted that all members $p_1, \ldots, p_n$ of a periodic orbit have the same stability type.

Let us focus for now on an unstable resonant orbit. There is a systematic way to obtain a "resonance zone", or as referred to above, the chaotic resonance zone, corresponding to the resonance, via the stable and unstable manifolds of $\mathcal{O}(p_n)$. We first must define a certain type of intersection between the stable and unstable manifolds of $\mathcal{O}(p_n)$. As the stable and unstable manifolds, $W^s(p_i)$ and $W^u(p_j)$, are 1-dimensional curves within the 2-dimensional Poincaré section Σ_C, they will generally intersect transversally in points.* An intersection point of the stable and unstable manifolds of the saddle-type periodic orbit $\mathcal{O}(p_n) = \{p_1, \ldots, p_n\}$ is termed a primary intersection point (PIP), denoted by q in Figure 3(a), if it meets the following criteria.

Definition 3. *Suppose $q \in W^u(p_i) \bigcap W^s(p_j)$, where $p_i, p_j \in \mathcal{O}(p_n)$, and let $U[p_i, q]$ denote the segment of $W^u(p_i)$ with endpoints p_i and q and $S[p_j, q]$ denote the segment of $W^s(p_j)$ with endpoints p_j and q. Then q is called a "primary intersection point (PIP)" if $U[p_i, q]$ intersects $S[p_j, q]$ only at the point q (and p_i if $i = j$).*

*A degenerate case occurs when $W^s(p_i) = W^u(p_j)$, a 1-dimensional intersection, but we will not consider this case.

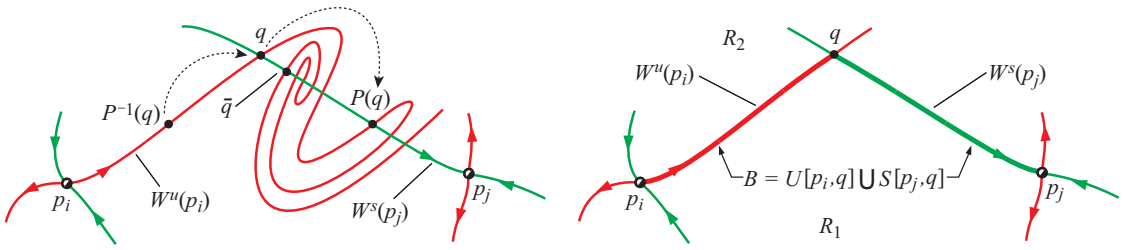

Figure 3: (a) The point q is a PIP, $\bar{q}$ is not a PIP (it is sometimes called a secondary intersection point). (b) A BIP q defining a local boundary B between two "sides", regions R_1 and R_2.

Since PIPs are intersections of stable and unstable invariant manifolds, it follows from the definition of stable/unstable invariant manifolds, that all the past and future iterates of a PIP are also PIPs. The following lemma is proved in Wiggins 1990.[9]

Lemma 1. *Suppose $q \in W^u(p_i) \bigcap W^s(p_j)$ is a PIP; then $P^k(q)$ is a PIP for all $k \in \mathbb{Z}$.*

We use PIPs to define *boundaries*, sometimes called separatrices, and subsequently resonance regions. Any PIP can be used to denote a local boundary.

Definition 4. *Suppose $W^u(p_i)$ and $W^s(p_j)$ intersect in the PIP q. Define $B \equiv U[p_i, q] \bigcup S[p_j, q]$ as a boundary between two "sides," region R_1 and region R_2. The PIP is then called a boundary intersection point (BIP).*

As a matter of convention, for a BIP we pick the PIP with the shortest arc-length of the manifolds, measured from the fixed points to the intersection point, i.e., the shortest arc-length for $U[p_i, q] \bigcup S[p_j, q]$. The BIP and the boundary B it defines allows for the local division of the Poincaré section Σ_C into distinct regions R_1 and R_2, as illustrated in Figure 3(b).

As there are always two branches each for a stable and unstable manifold, we can identify both a "top" and "bottom" boundary. We denote the two branches of the unstable manifold of a period-n point p_i by $W^u_+(p_i)$ and $W^u_-(p_i)$, and similarly for p_j. Referring to Figure 4, we suppose that $W^u_+(p_i)$ intersects $W^s_+(p_j)$ and $W^s_-(p_i)$ intersects $W^u_-(p_j)$. Choosing BIPs $q^+ \in W^u_+(p_i) \bigcap W^s_+(p_j)$ and $q^- \in W^s_-(p_i) \bigcap W^u_-(p_j)$, we can identify boundaries B^+ and B^- that define a closed region R_1, which we refer to as a *resonance region*.

Within our cylindrical Poincaré section Σ_C, we can have multiple resonance regions, as shown in Figure 5. For our purposes, we will label the "width" of a (chaotic) resonance region as the distance between the BIPs with the maximum and minimum semi-major axes, the dashed lines in Figure 5.

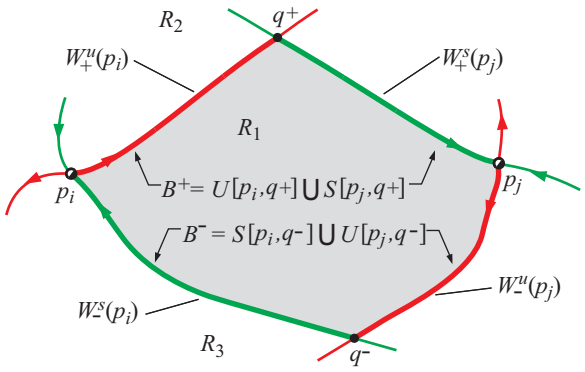

Figure 4: Construction of a top and bottom boundary to a resonance region R_1.

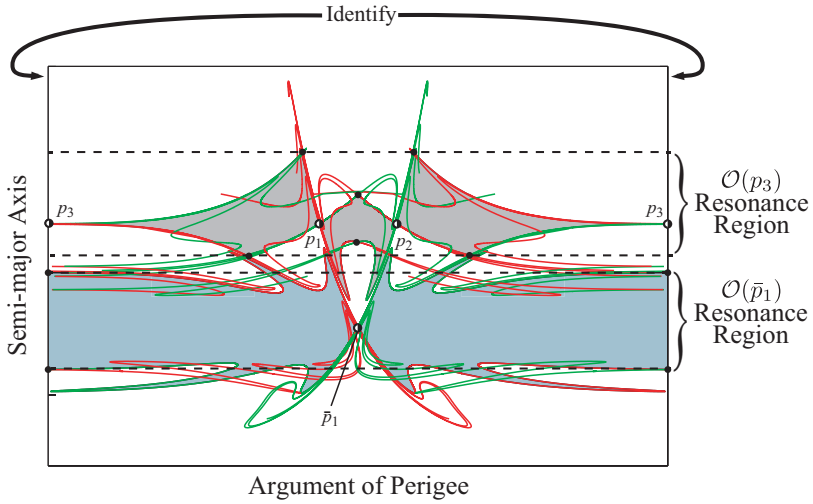

Figure 5: Example calculation[14] of two neighboring resonance regions corresponding to neighboring resonant orbits, a period-3 orbit $\mathcal{O}(p_3) = \{p_1, p_2, p_3\}$ and a period-1 orbit $\mathcal{O}(\bar{p}_1) = \{\bar{p}_1\}$. The "identify" reminds us that the horizontal axis, the argument of perigee, is an angle and therefore we are looking at a "cut" and "unfolded" portion of the cylindrical phase space Σ_C.

Resonance regions represent the dynamical "sphere of influence" of a particular resonance. In the PCR3BP, they contain within them the corresponding stable resonant periodic orbit and the surrounding stable quasi-periodic orbits, the librational resonant tori. Outside of the largest (outermost) librational torus, there is a "stochastic" or chaotic layer. This is illustrated in Figure 6. The dynamics of motion into and out of the resonance region are determined by lobe dynamics not addressed here,[14] but documented elsewhere.[6, 15–18]

Intersections between stable and unstable invariant manifolds of different periodic orbits can occur. For example, suppose $\mathcal{O}(p_n)$ and $\mathcal{O}(\bar{p}_m)$ correspond to two different continuous unstable periodic trajectories in the PCR3BP, as in Figure 5. Unless constrained by other barriers within Σ_C, such as rotational invariant curves (RICs)[3, 5, 19]–which are quasiperiodic KAM tori which block transport along semi-major axis in the cylindrical phase space of Σ_C — it is possible for there to be intersections between their stable and unstable manifolds, denoted as *heteroclinic* points.

Definition 5. *A point $q \in \Sigma_C$ is called a heteroclinic point if $q \in W^u(p_i) \bigcap W^s(\bar{p}_j)$. Such a point corresponds to a continuous heteroclinic trajectory in $\mathcal{M}_C$, which is backward asymptotic to $\mathcal{O}(p)$ and forward asymptotic to $\mathcal{O}(\bar{p})$.*

One can see several such heteroclinic points in Figure 5, although they are not called out. Heteroclinic transfers between unstable resonance orbits will be explored in Section VIII.

IV. RESONANCE IN XGEO

Resonances in celestial mechanics result from gravitational interactions among celestial bodies, where their orbital periods create specific ratios. For instance, a 2:1 resonance signifies that one body completes two orbits for every single orbit completed by another, thereby influencing the stability and evolutionary trajectories of orbits over extended duration; see Figure 7.

Of particular interest for space domain awareness (SDA) within cislunar xGEO space are recurrent pathways between Earth and the Moon's orbit. Resonant orbits, being inherently periodic, have a rich history in mission-design applications, particularly within the Earth-Moon system.

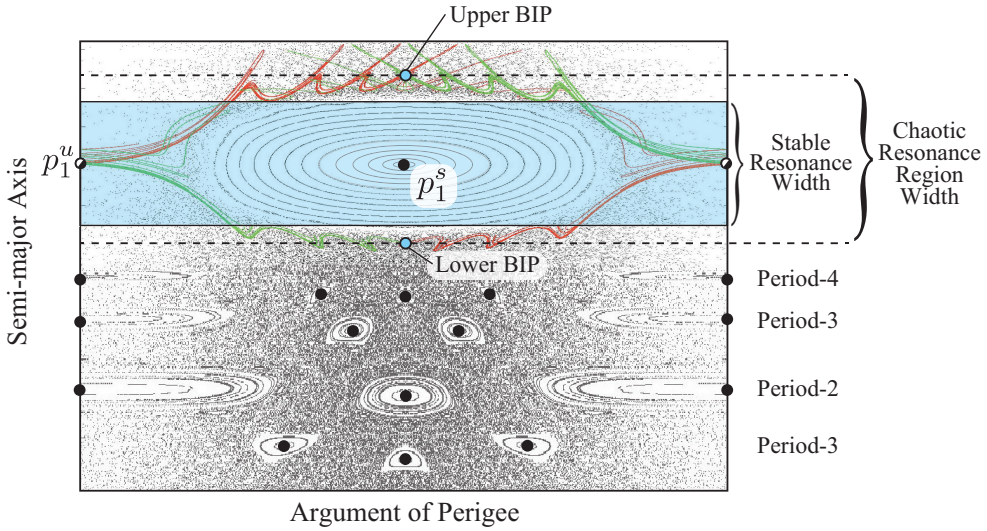

Figure 6: Example calculation on a Poincaré section at perigee, Σ_C, showing background points; initial conditions followed over several iterates of the map P. One sees regions of concentric closed curves, the quasiperiodic librational tori of various stable islands, grouped into horizontal bands at nearly constant semi-major axis; these are the stable resonances. Outside of these closed curves, an almost uniform distribution of scattershot points representing a connected chaotic sea is shown. Within this chaotic sea are unstable resonant periodic orbits, and their stable and unstable manifolds, which reveal the template of chaotic motion. For instance, the period-1 point p_1^u, shown near the top, is the unstable resonant periodic orbit counterpart of the stable resonant periodic orbit p_1^s. The stable resonance width is given by the outermost closed curve of the stable resonance, while the larger chaotic resonant region width is given by the semi-major axis width between the upper and lower BIP. Other stable period-n points corresponding to other resonances are also shown.

A mean-motion resonance denoted as k:k_m is characterized by the ratio of orbital periods where k and k_m denote coprime positive integers representing the number of spacecraft and Moon geocentric orbits completed with respect to an Earth-centered inertial frame. In this paper, we study interior resonances, where $k > k_m$. Expressed in terms of the inertial-frame period of the spacecraft, T, and the sidereal period of the Moon, we have an approximate relationship, $T/T_m \approx k_m/k$. When observed within the context of the CR3BP, resonant orbits do not adhere strictly to the integer ratio k_m/k, thus $T/T_m \approx k_m/k$ is approximate. Instead, a spacecraft completes approximately k revolutions around the Earth in the time it takes the Moon to complete k_m revolutions. In terms of the Poincaré map and section pair described above, (P, Σ_C), a resonant orbit is a period-m orbit which takes approximately n sidereal lunar periods. These orbits can be found via differential-correction procedures that are well-known in the literature.[14]

Resonant orbits can be categorized as either stable (characterized for interior resonances by a perigee oriented towards the Moon viewed in the rotating frame) or unstable (for interior resonances, having an apogee oriented towards the Moon). Unstable resonant orbits can be used in mission design for transfer scenarios, while stable resonant orbits, as demonstrated by missions such as IBEX and TESS, ensure sustained operational stability. For example, IBEX transitioned into a stable 3:1 resonant orbit following its launch, contributing to its prolonged mission duration.[20] Similarly, TESS has maintained a stable 2:1 resonant orbit since its inception via a lunar flyby.[21]

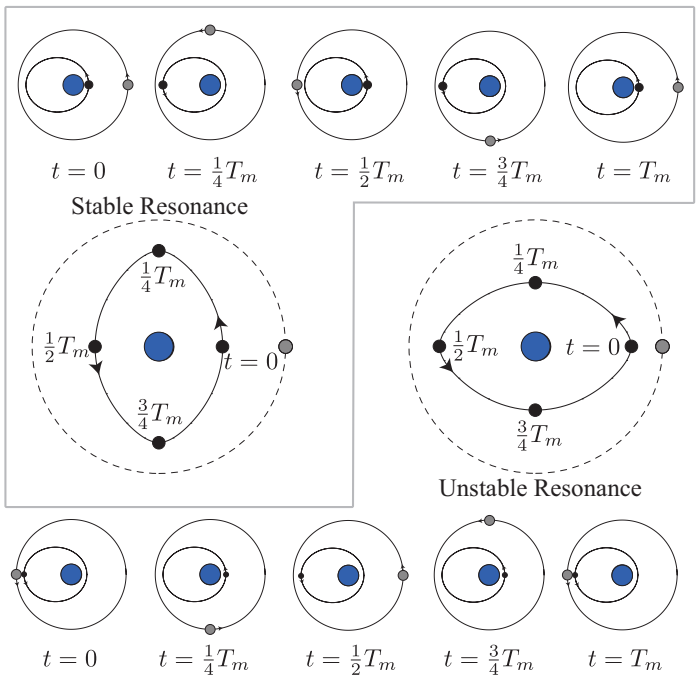

Figure 7: The geometry of mean-motion resonances. (Upper left) Consider a spacecraft in a 2:1 resonance with the Moon. The relative positions of the Moon (gray circle) and the spacecraft (black circle) for the stable resonance when their orbital periods are in a ratio of 2:1. Along the top, T_m is the period of the Moon's orbit then the diagrams illustrate the configurations at times, from left to right, $t = 0$, $t = \frac{1}{4}T_m$, $t = \frac{1}{2}T_m$, $t = \frac{3}{4}T_m$, $t = T_m$, and on the left, shown schematically in the rotating frame. Along the bottom, we illustrate an unstable resonance the same way, and on the right, in the rotating frame. Notice the stable resonance has a perigee in the direction of the Moon and the unstable resonance has an apogee in the direction of the Moon.

V. UNSTABLE PERIODIC ORBITS AND MANIFOLDS

In the PCR3BP, to understand the structure of unstable resonant orbit families and the heteroclinic dynamics induced by them, one needs to compute the corresponding periodic orbits as well as their stable/unstable manifolds. To compute a family of k:k_m unstable periodic orbits in the Earth-Moon PCR3BP, we start with an orbit state from the Earth Kepler problem having semi-major axis a such that $(a/a_m)^{3/2} = (k_m/k)$ and initial argument of periapse and true anomaly both π (for the interior MMRs considered in this study). This orbit will be symmetric about the x-axis and will also be periodic in the rotating Kepler problem (i.e., PCR3BP with $\mu = 0$). Thus, the method of perpendicular x-axis crossings can be used to numerically continue this Keplerian orbit to the true value of $\mu = 1.2150584270571545 \times 10^{-2}$ for the Earth-Moon system; see, for example, Section 2.6.6.2 of Parker and Anderson[22] for details of this method. The same method is then used to continue the resulting PCR3BP orbit through the rest of its orbit family, using the perpendicular orbit x-intercept as the continuation parameter.

Once the periodic orbits in a family k:k_m have been computed, the computation of their stable/unstable manifolds is carried out. In particular, we compute the intersection of these manifolds with the previously mentioned perigee Poincaré surface of section. Such sections have been used by, e.g., Ross and Scheeres[5] and Howell et al.[23] as well; they have better transversality to the

PCR3BP flow as compared to other commonly used sections such as $y = 0$. When using such a section, however, the periodic orbit intersection points with the section are not fixed points of the section's Poincaré map, but become period-k orbits under the map, as discussed in Section III. This is because such an k:k_m orbit passes through periapse (apoapse) k times during one period, which takes approximately k_m lunar sidereal periods.

The portions of the periodic orbit stable/unstable manifolds lying in the chosen Poincaré section will correspond to 1D curves — one curve for each of the period-k points lying in the section. To help accurately compute the manifolds, we extended to the period-k iteration orbit case the second author's previously developed parameterization method[24,25] for computing Taylor-series approximations of periodic orbit stable/unstable manifolds; this extension also incorporates many methods from the second author's previous work[26] on computing manifolds of invariant tori. Although a full description is beyond the scope of this paper, in short, we solve for a function $W : \{0, \ldots, k-1\} \times \mathbb{R} \to \mathbb{R}^4 \subset \mathcal{M}_C$ such that,

$$\phi_{\tau(i)}(W(i,s)) = W(i+1 \mod k, \lambda s) \quad i \in \{0, \ldots, k-1\}, \tag{8}$$

where $\phi_t(X)$ is the PCR3BP flow map of a point $X \in \mathcal{M}$ by time t, $\tau(i)$ are the times between the ith and $(i+1)$th periapse passes of the periodic orbit being considered, and λ is the kth root of the monodromy matrix eigenvalue corresponding to the stable/unstable manifold. Equation (8) can be solved recursively by expressing W as a set of Taylor series depending on the integer i,

$$W(i,s) = \sum_{m=0}^{\infty} W_m(i) s^m \quad i \in \{0, \ldots, k-1\}, \tag{9}$$

where $W_0(i) = p_{i+1}$ are the periapse period-k points of the periodic orbit, and $W_1(i)$ are scaled eigenvectors of the periodic orbit monodromy matrix at each of its periapse passages, with $W_m(i)s^m$ for $m \geq 2$ corresponding to higher order terms in the stable/unstable manifold approximation.

The k curves parameterized by W lie near but not on the periapse section of interest. Thus, to finally compute the manifolds on the section, one simply numerically integrates dense grids of points from those curves either backwards or forwards to the section. Then, further applications of the Poincaré map either forwards or backwards in time are used to respectively globalize the full unstable and stable manifolds. As usual, for each fixed Jacobi constant value C, one can plot these Poincaré map manifolds of various orbits at that C value using just 2D coordinates on Σ_C. Intersections of the 1D manifold curves, $\{W_{\pm}^{u,s}(p_i)\}$, will provide the geometry (e.g., PIPs, BIPs, homoclinic points, heteroclinic points) as discussed in Section III.

VI. SEMI-ANALYTICAL APPROACH TO IDENTIFY RESONANCE WIDTHS

Standard tools have been developed in celestial mechanics to calculate the width (strength) and location of MMRs, under the perturbed Hamiltonian formulation.[1,27,28] They all invariably employ an expansion of the Hamiltonian around each resonant location and a *canonical transformation* to reduce the Hamiltonian to a system with only one single harmonic (i.e., normal-form reduction). While the mathematical developments here are straightforward, they can be algebraically quite complicated, especially for distant xGEO orbits of high eccentricity and inclination.

The Hamiltonian describing the resonant dynamics is,

$$\mathcal{K}(a,\sigma) = -\frac{\mu_e}{2a} - n_m \frac{k_m}{k}\sqrt{\mu_e a} - \mathcal{R}(a,\sigma), \quad \mathcal{R}(a,\sigma) = \frac{1}{2\pi k}\int_0^{2\pi k} R(\lambda_m, \lambda(\lambda,\sigma))\,\mathrm{d}\lambda_m, \tag{10}$$

where $\mu_e = Gm_e$ is the Earth's gravitational parameter, $n_m = \sqrt{\mu_e/a_m^3}$ is the Moon's mean motion, λ_m and λ are the Moon and satellite mean longitudes, respectively, and R is the Moon's disturbing function,

$$R = \mu_m \left(\frac{1}{|\boldsymbol{r}_m - \boldsymbol{r}|} - \frac{\boldsymbol{r} \cdot \boldsymbol{r}_m}{r_m^3} \right). \tag{11}$$

The resonant disturbing function, $\mathcal{R}(a, \sigma)$, can be written as a series expansion of cosines whose critical arguments are of the type,

$$\sigma = k_p \lambda_m - k\lambda + \gamma, \tag{12}$$

where γ is a slowly evolving angle defined by a linear combination of the longitudes of the ascending nodes Ω and longitudes of perigee $\varpi = \Omega + \omega$ of the satellite and Moon. Gallardo[10,11] uses a numerical computation for the averaging in Eq. (10), assuming fixed coplanar orbits for both the spacecraft and the Moon, and taking for the spacecraft the semi-major axis corresponding to the nominal position of the resonance, during the period of time in which the integral is calculated. This is justified in the asteroid case by the otherwise slow evolution timescale of (e, i, ω, Ω), as compared to the oscillations of a and σ. Another assumption is that the perturber's orbit is circular.

For the Earth-Moon system, the resonance widths using Gallardo's algorithm are shown in osculating semi-major axis-eccentricity (a, e) space in Figure 8, with their qualitative phase-space structure generally resembling those in the small-body context.[29] Time histories of historic and current cataloged xGEO space objects, based on TLE data, are also overlaid. Notably, the computed widths appear to dramatically underestimate the 3:1 and 2:1 stable resonance zones, where IBEX and TESS are respectively located (labeled in Figure 12).

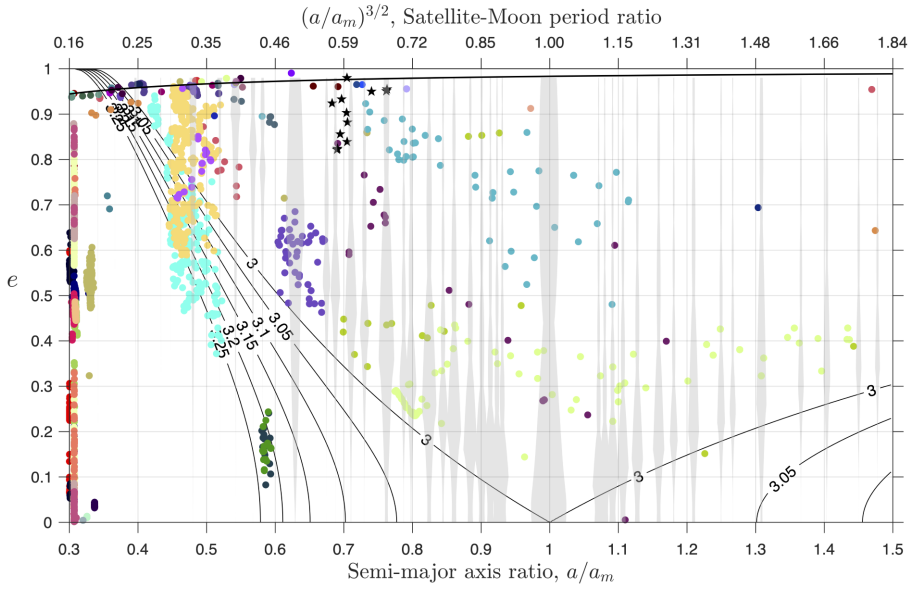

Figure 8: The historic and current cataloged xGEO space objects projected onto the semi-major axis-eccentricity (a, e) plane, superimposed on the atlas of MMRs, where each color corresponds to the two-line element (TLE) time histories of individual objects (www.space-track.org, Assessed 10 Mar. 2023). The contours of constant Tisserand parameter, shown in black, and Gallardo's analytical approximation of widths of predominant MMRs (gray) are both computed assuming that the objects' and Moon's orbit are coplanar.

VII. DIRECT IDENTIFICATION OF RESONANCE WIDTHS AND CHAOTIC ZONES

We calculate the Poincaré section Σ_C for a range of Jacobi constants which reveals various resonances; see the (a, g)-plane in Figure 9, where, recall, g is the argument of perigee in the rotating frame. The prominent resonances are the 2:1, 3:1 and 4:1 MMRs; the stable resonances are particularly apparent as "islands" of concentric closed curves surrounding center points that are stable period-2, period-3, and period-4 orbits, respectively. The closed curves surrounding the stable fixed points are stable quasi-periodic librational tori (recall Section III). Surrounding these resonance islands are regions of chaos. These regions are not featureless. Instead, the template of the motion is given by the corresponding unstable MMR periodic orbits, which appear as saddle-type period-k points on the Poincaré section Σ_C. Using the method of Section V, their stable and unstable manifolds are computed. The stable and unstable manifolds intersect to form homoclinic and heteroclinic tangles, which provide the paradigm with which to understand chaos in the CR3BP.[4,30]

The region of existence of a particular periodic resonance can be identified by examining the Poincaré section, which also reveals the strength (width) of the resonance. Resonance widths were defined in Section III (see Figure 6), and are shown for the 3:1 and 2:1 MMRs on Poincaré maps computed for $C = 3.00, 3.05, 3.10, 3.15$ in Figure 9.

The influence of the resonance region extends beyond the outermost stable resonance librational torus regions to the "separatrix", the boundary formed by the intersection of stable and unstable manifolds described in Section III (see Figure 5). Focusing on the MMR bands, we use the methods of Section III to identify BIPs and designate the boundary of the (chaotic) resonance region. BIPs defining the chaotic zones are depicted on the same Poincaré maps in Figure 9.

While the resonances are identified and depicted in (a, g) space, we would like to also depict them in the (a, e) plane, for comparison with the space objects and analytical resonant widths shown in Figure 8. The Poincaré section points, which are actually 3-dimensional points (a, e, g) for

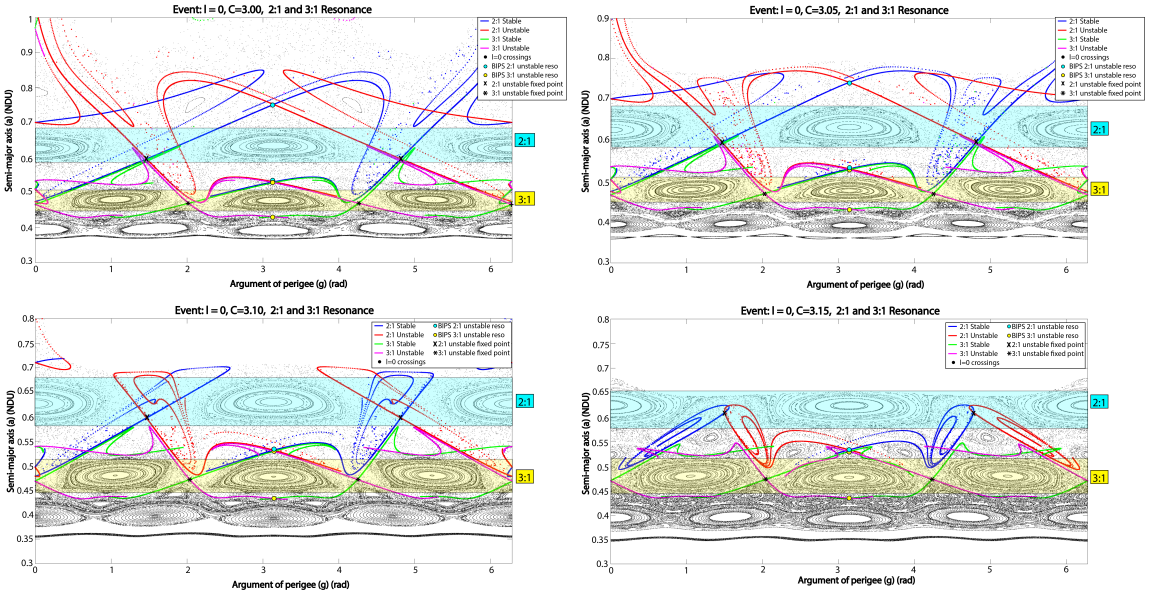

Figure 9: Poincaré sections Σ_C for $C = 3.00, 3.05, 3.10$, and 3.15, depicting resonance widths of the stable 2:1 and 3:1 MMRs and BIPs of the corresponding unstable periodic resonance orbits forming chaotic zones for the 2:1 and 3:1 MMRs.

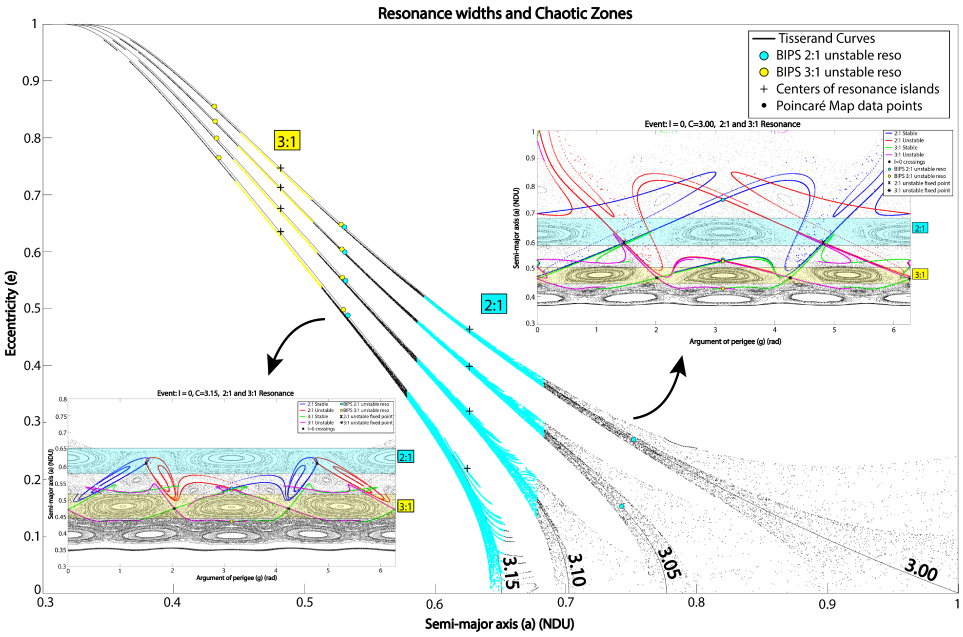

Figure 10: Resonance widths and resonance regions for 2:1 and 3:1 resonance for $C = 3.00, 3.05, 3.10, 3.15$ (going from top curve to bottom) shown in the (a, e) plane. The '+' on the widths mark the location of the stable periodic orbits (center). The filled circles on the Tisserand curves are the location of the BIPs, representing the resonance's region of influence.

each C, can be projected into the (a, e) plane as in Figure 10, where stable resonance widths and the BIPs bounding the resonance zones are delineated. As noted in Section II, Tisserand curves are an approximation to the projection of an energy surface $\mathcal{M}_C$ onto the (a, e) plane. For each Jacobi constant C in Figure 10, we also show the Tisserand curve, merely to show the agreement, particularly for smaller semi-major axes.

The results in Figure 10 illustrate our method, but the number of Jacobi constants is sparse. To get a fuller picture of the (stable) resonance widths and the (chaotic) resonance regions, Poincaré sections were computed for Jacobi constant values C ranging from 2.50 to 3.42 in increments of $\Delta C = 0.02$. As shown in Figure 11, the Poincaré section points were projected onto the (a, e) plane, marking resonance widths and chaotic zones (via BIPs) for the 2:1 and 3:1 resonances. The widths obtained by using the full CR3BP model are larger than those computed using Gallardo's algorithm. The influence of the resonance regions is more spread out. The width, particularly for the 2:1 resonance, does not taper towards $e = 0$ as compared to Gallardo's approximation. The Gallardo's width for 2:1 resonance does not mark the center of the stable island, i.e, the 2:1 stable periodic orbit computed in the CR3BP. Moreover, the shape of the 2:1 resonance does not show the characteristic shape seen in other resonance width computations based on the CR3BP[2,31] — a largest width near some eccentricity $0.3 \leq e \leq 0.7$ tapering to significantly smaller widths as e approaches 0 and 1. We note that earlier work tended to assume that resonance widths should be along lines of constant semi-major axis in the (a, e) plane[31] which does not consider the 'tilt' of the energy surface (as approximated by Tisserand curves).

The 2:1 and 3:1 resonance regions, as represented by BIPs, nearly touch in the region between them, indicating possible heteroclinic connections, discussed in Section VIII. Taken together, the 2:1 and 3:1 resonance regions span approximately 0.3 NDU (about 115,000 km) in semi-major

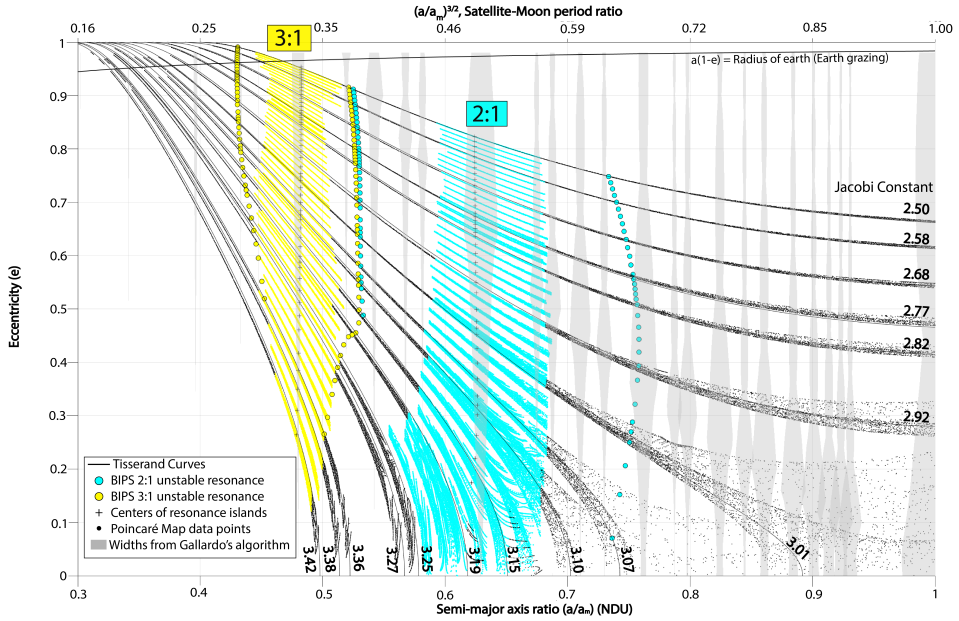

Figure 11: Resonance widths and chaotic resonance zones for 2:1 and 3:1 resonance for $C = 2.50$ to $C = 3.42$ with increments of $\Delta C = 0.02$, overlapped on Gallardo's widths

axis, which encompasses numerous higher-order resonances, suggesting the potential for multiple free transfers between different order resonances.

As done previously in Figure 8, time histories of historic and current cataloged xGEO space objects are overlaid in Figure 12. The CR3BP resonance widths effectively encompass several

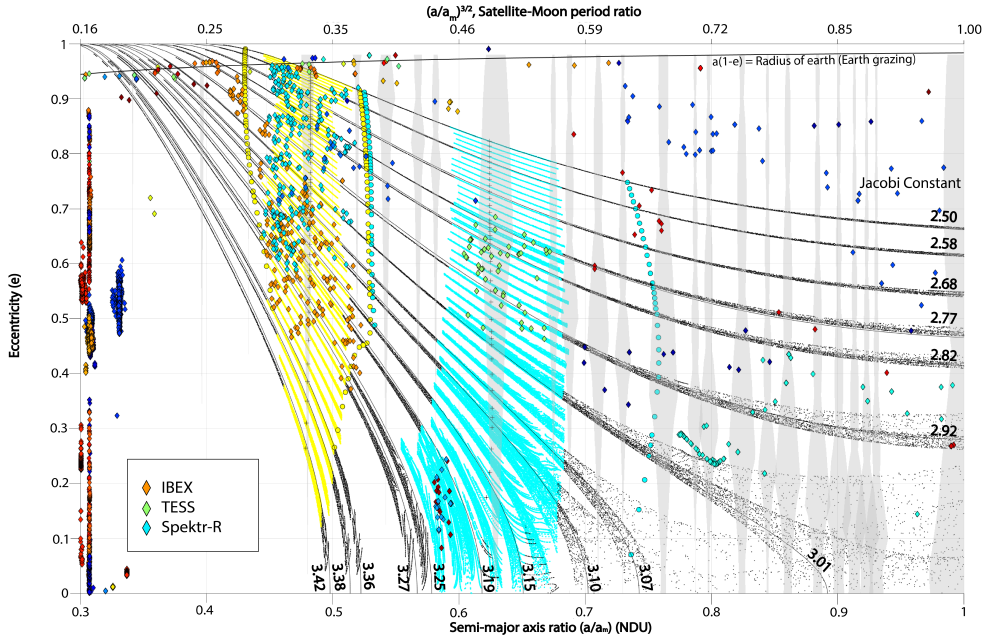

Figure 12: TLEs of xGEO space objects (from Figure 8) superimposed on Gallardo's widths and the CR3BP widths. The CR3BP resonance widths correctly capture the spread of space assets in the 2:1 and 3:1 stable resonance zones, namely IBEX, TESS and Spektr-R.

spacecraft, such as IBEX, TESS, and Spektr-R. In contrast, the narrow semi-analytical, resonance-zone approximation inadequately represents the spacecrafts' locations. Notably, the PCR3BP can accurately discern the dynamics of even non-coplanar spacecraft like IBEX, underscoring its utility in providing fundamental insights into spacecraft dynamics in cislunar space. Utilizing these resonance widths facilitates the determination of whether a spacecraft is within a stable or chaotic orbital regime, thereby aiding in mission analysis and prediction of its future orbital evolution.

For instance, IBEX's nominal orbit exhibited chaotic behavior due to lunar perturbations, prompting a transition to a stable resonant orbit with the Moon.[20] A comprehensive understanding of chaotic dynamics in such environments would have been valuable during the mission's early design phases. This understanding has partly informed the orbital design of missions like TESS.[21] Although significant challenges remain in comprehending lunar secular and mean-motion resonances, progress in discerning the influence of specific resonances, such as the 2:1 and 3:1 MMRs, through the PCR3BP, contributes to advancing our understanding of these lunar resonances.

VIII. HETEROCLINIC CONNECTION BETWEEN RESONANCES

The Poincaré maps (Figure 13) reveal intermingling of the stable and unstable manifolds of 2:1 and 3:1 unstable resonant orbits while the 4:1 resonance is disconnected from the two, due to a RIC (barrier) that prevents chaotic transport[3,5,19] even at lower Jacobi constants (higher energies).

To study heteroclinic connections between 2:1 and 3:1 resonances, intersections are identified between the unstable manifold of the 3:1 unstable periodic orbit and the stable manifold of the 2:1 unstable periodic orbit. Similarly, intersections are found between the unstable manifold of the 2:1 unstable periodic orbit and the stable manifolds of the 3:1 unstable periodic orbit. This suggests

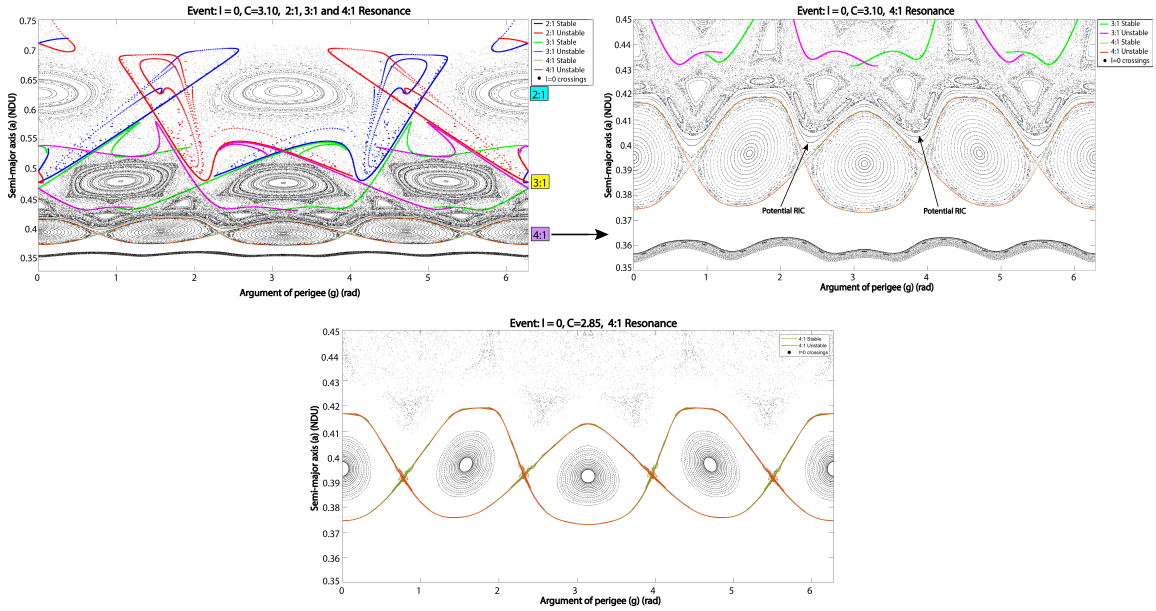

Figure 13: Top panel: $C = 3.10$, no connection observed between 3:1 and 4:1 resonances. Numerical evidence suggests the 4:1 resonance region is blocked from connections to the main connected chaotic component of Σ_C (which includes the 3:1 and 2:1 resonance regions) via a barrier, a rotationally invariant circle (RIC).[19] Bottom panel: $C = 2.85$ marks one of the highest-energy, most eccentric unstable prograde orbits in the 4:1 family. Blocked by RICs, its manifolds still show no signs of any heteroclinic jumps to other resonances.

the existence of direct transfer trajectories between the two resonance orbits, enabling a change in semi-major axis value without fuel expenditure.

Heteroclinic transfers are computed for various Jacobi constants. The selection of the intersection point of stable and unstable manifolds determines the type of transfer trajectory. Our study examines two types of transfer trajectories: type 1 (short-duration) and type 2 (long-duration). For transfer type 1, the intersection point selected is marked as 9 (Figure 14), which determines a direct, shortest-duration transfer between the two resonances. This intersection point ceases to exist for $C \geq 3.09$,

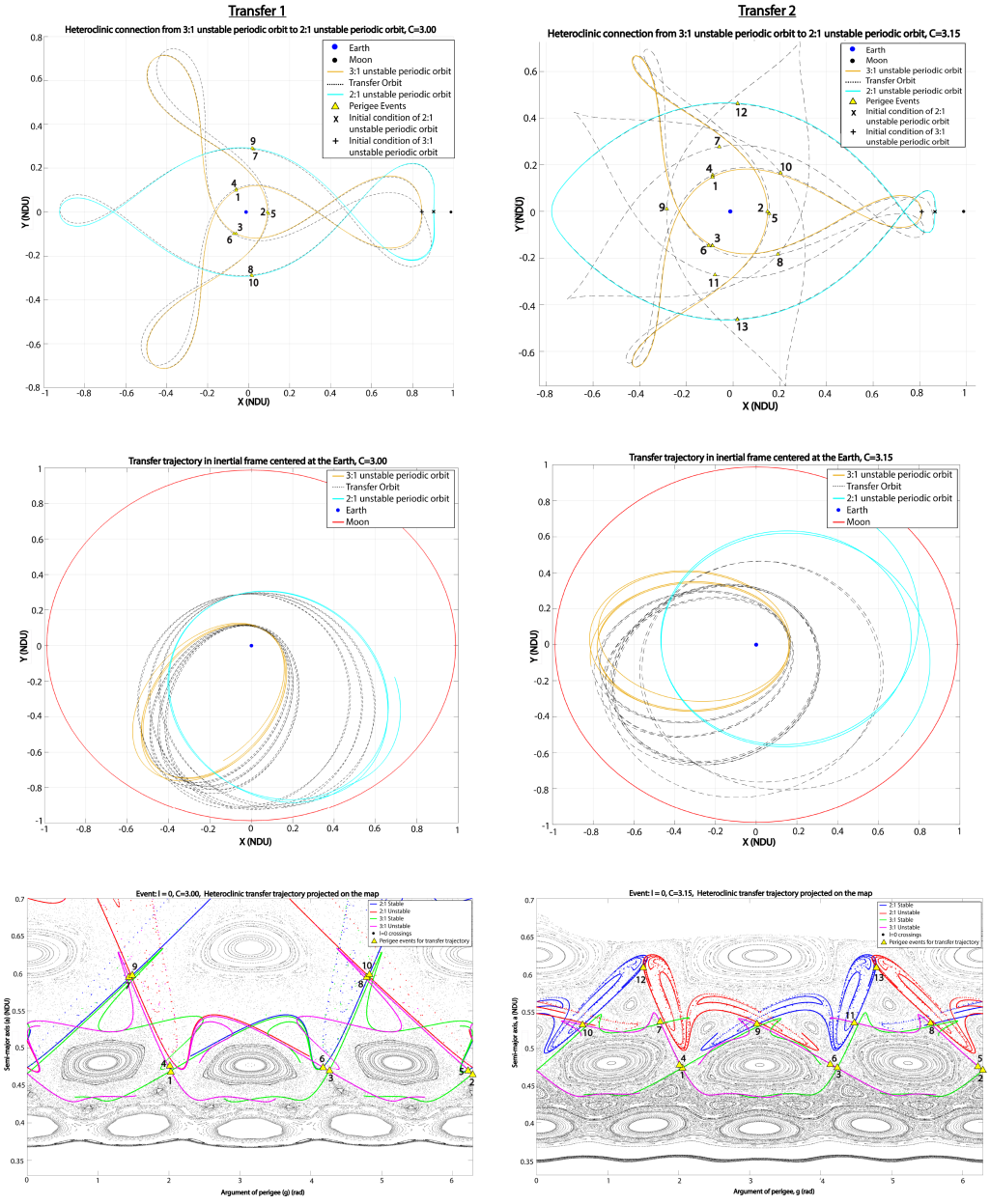

Figure 14: Two types of heteroclinic transfer trajectories between 3:1 and 2:1 resonances. Type 1 (short duration) for $C = 3.00$ (left) and type 2 (long duration) for $C = 3.15$ (right).

due to lower energy, resulting in reduced chaos, and consequently, the interaction of stable and unstable manifolds leading to direct transfer ceases to exist. The intersection point selected for transfer type 2 is marked as 10 (Figure 14), representing a longer-duration transfer that transitions from the 3:1 to the 2:1 unstable periodic orbit via an intermediary 5:2 resonance.

Precisely determining the intersection point requires significant precision; therefore, points on the unstable 3:1 manifold and stable 2:1 manifold that are the closest ($\approx 10^{-5}$ NDU) to each other are considered to depict the transfer trajectory. The point on the unstable manifold is followed backward in time, while the point on the stable manifold is followed forwards in time until both reach within $\approx 10^{-6}$ NDU distance near their respective unstable fixed points. In theory, the exact attainment of the fixed points necessitates an infinite time duration due to asymptotic convergence. Therefore, for practical operational applications and the computation of realistic transfer durations, transfer times are determined by observing the changes in the averaged semi-major axis value as the trajectory transitions between resonances. Operationally, an orbit is considered a viable transfer once it approaches sufficiently close to the periodic orbit.

The time required for transfer from one fixed point to another is computed for a range of Jacobi constants. For $2.50 \leq C \leq 3.07$, the direct transfer trajectory from the 3:1 to the 2:1 resonance takes approximately 28-29 days. This trajectory ceases to exist for $C \geq 3.09$. However, a longer duration transfer trajectory exists that passes from the 3:1 to the 2:1 resonance via an intermediate 5:2 resonance and takes approximately 56-57 days. These transfer times are heuristic, depending on how one defines the beginning and end of the transfer. The results indicate that change in transfer time remains nearly insignificant to changes in the Jacobi constant for both types of transfers, respectively. Also note that if a transfer is found from the 3:1 to the 2:1 resonant orbit, then a transfer from the 2:1 to the 3:1 is found via the time-reversal symmetry of the CR3BP equations, Eq. (1).

IX. CONNECTIONS WITH L1 TUBES

As first noticed in Koon et al. 2000[4] and elaborated upon in 2001[32] and 2003,[33] intersections between "lobes" related to invariant manifold of unstable MMR periodic orbits and "tubes" associated with L_1 Lyapunov orbits can be used to design low-energy trajectories between Earth orbits and lunar orbits (also recently used by Hiraiwa et al. 2024[7]). The first Poincaré cut of a the L_1 Lyapunov orbit stable manifold on Σ_C is denoted as an "exit" from Σ_C in the Earth realm. All trajectories entering it must emerge in an "entrance" in the Moon realm, as illustrated in Figure 15.

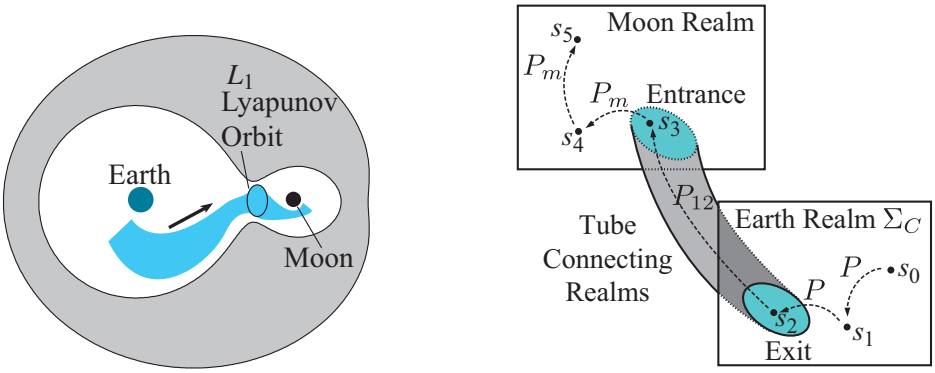

Figure 15: Tube dynamics: an exit leaving the Earth realm Poincaré section Σ_C, taking trajectories to the Moon realm.

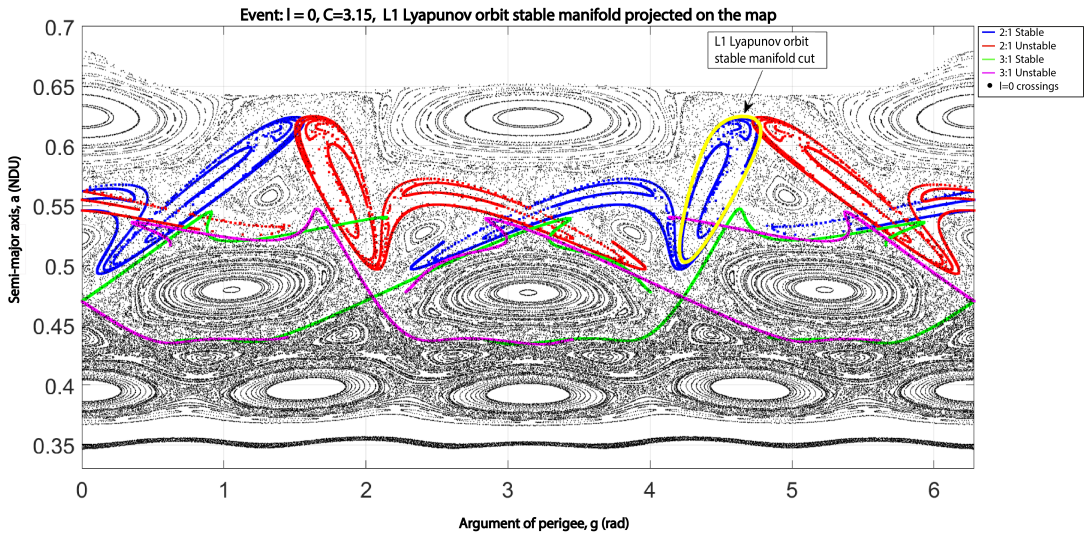

Figure 16: Poincaré section Σ_C for $C = 3.15$ with L_1 Lyapunov orbit stable manifold (the Earth realm "exit" as in Figure 15) overlaying the 2:1 and 3:1 unstable resonance manifolds.

In our numerical investigations, we have come across a strong interaction between the invariant manifolds of the 2:1 unstable periodic orbit and the stable/unstable tubes (first Poincaré cut[4]) for a certain range of Jacobi constant. One such case is shown in Figure 16.

The 'swirling' of manifolds seen inside the L_1 Lyapunov orbit cuts are a consequence of trajectories 'exiting' the Poincaré section Σ_C in the Earth realm, entering the Moon realm, and then re-emerging in the Earth realm. This leads to numerical challenges, encountered in other contexts, particularly atomic physics and chemistry.[34]

X. DISCUSSION AND FUTURE WORK

Poincaré sections at perigee provide a detailed depiction of the dynamical structure within cislunar space, highlighting both stable islands and chaotic regions, all depicted in geocentric orbital elements, which are immensely useful for cislunar space. Our results highlight the pronounced impact of the 2:1 and 3:1 resonances, with a special focus on stable resonance widths and the expansive unstable chaotic resonance zones. Our findings underscore limitations in semi-analytical approaches (i.e., Gallardo's algorithm[1]) used to assess the influence of MMRs in cislunar space, revealing that the CR3BP model more accurately predicts that these resonances exhibit broader widths, with a structure hitherto unseen in other astronomical systems, which involve much small mass ratios μ (e.g., the asteroid and Kuiper belts). Analysis of unstable periodic resonant orbits has identified regions of chaotic dynamics characterized by interactions between stable and unstable manifolds. Specifically, we have quantified the extent of chaotic zones associated with the 2:1 and 3:1 lunar MMRs, and depicted them in geocentric orbital elements. Furthermore, by comparing with historic and current cataloged xGEO space objects, based on TLEs, we find that our larger regions provide a better fit with objects known to be in the 3:1 and 2:1, compared with previous approaches, particularly the IBEX and TESS spacecraft, respectively, which highlights the Earth-Moon system as an astrodynamics laboratory.[35] Employing these newly established resonance widths and chaotic zones for a wider range of MMRs — an atlas of MMRs — allows for an enhanced determination of whether space assets reside in stable or unstable orbital regimes.

Additionally, our study demonstrates the potential for heteroclinic connections between 3:1 and 2:1 resonances within feasible time scales (operational transfer times on the order of a month), while no such connections exist for the 4:1 resonance, due to dynamical barriers in the phase space. This examination of MMRs using a global dynamics approach (using the CR3BP as model) enhances our understanding of the intricate dynamics of xGEO objects, with implications for mission analysis, mission design, cislunar SDA and operations. Future research directions will focus on refining methodologies to precisely determine resonance widths and chaotic zones, moving beyond qualitative assessments. Additionally, we aim to explore the influence of 3-dimensionality (e.g., inclination), a significant factor contributing to the presence of secular resonances. Further investigation will involve studying chaotic transport across resonances through analysis of lobe dynamics and flux across chaotic regions. Moreover, we intend to investigate the interaction effects resulting from the overlap of the stable/unstable manifold tubes of the L_1 Lyapunov orbit with that of significant lunar resonances (e.g., 2:1, 5:2, and 3:1).

Acknowledgments

BK was supported by the National Science Foundation under award no. DMS-2202994. Part of this research was carried out at the Jet Propulsion Laboratory, California Institute of Technology, under a contract with the National Aeronautics and Space Administration.

REFERENCES

[1] T. Gallardo, "Atlas of the mean motion resonances in the Solar System," *Icarus*, Vol. 184, No. 1, 2006, pp. 29–38.
[2] R. Malhotra and N. Zhang, "On the divergence of first-order resonance widths at low eccentricities," *Monthly Notices of the Royal Astronomical Society*, Vol. 496, No. 3, 2020, pp. 3152–3160.
[3] J. D. Meiss, "Symplectic maps, variational principles, and transport," *Rev. Mod. Phys.*, Vol. 64, 1992, pp. 795–848.
[4] W. S. Koon, M. W. Lo, J. E. Marsden, and S. D. Ross, "Heteroclinic connections between periodic orbits and resonance transitions in celestial mechanics," *Chaos*, Vol. 10, 2000, pp. 427–469.
[5] S. D. Ross and D. J. Scheeres, "Multiple gravity assists, capture, and escape in the restricted three-body problem," *SIAM Journal on Applied Dynamical Systems*, Vol. 6, No. 3, 2007, pp. 576–596, 10.1137/060663374.
[6] S. Naik, F. Lekien, and S. D. Ross, "Computational method for phase space transport with applications to lobe dynamics and rate of escape," *Regular and Chaotic Dynamics*, Vol. 22, May 2017, pp. 272–297, 10.1134/S1560354717030078.
[7] N. Hiraiwa, M. Bando, I. Nisoli, and Y. Sato, "Designing robust trajectories by lobe dynamics in low-dimensional Hamiltonian systems," *Physical Review Research*, Vol. 6, No. 2, 2024, p. L022046.
[8] R. S. MacKay, J. D. Meiss, and I. C. Percival, "Transport in Hamiltonian systems," *Physica D*, Vol. 13, 1984, pp. 55–81.
[9] S. Wiggins, "On the geometry of transport in phase space I. Transport in k-degree-of-freedom Hamiltonian systems, $2 \leq k \leq \infty$," *Physica D: Nonlinear Phenomena*, Vol. 44, No. 3, 1990, pp. 471–501.
[10] T. Gallardo, "Strength, stability and three dimensional structure of mean-motion resonances in the Solar System," *Icarus*, Vol. 317, 2019, pp. 121—134.
[11] T. Gallardo, "Three-dimensional structure of mean-motion resonances beyond Neptune," *Celestial Mechanics and Dynamical Astronomy*, Vol. 132, 2020, p. 9 (26 pp.).
[12] J. D. Meiss and E. Ott, "Markov tree model of transport in area-preserving maps," *Physica D*, Vol. 20, 1986, pp. 387–402.
[13] C. G. Schroer and E. Ott, "Targeting in Hamiltonian systems that have mixed regular/chaotic phase spaces," *Chaos*, Vol. 7, 1997, pp. 512–519.
[14] W. S. Koon, M. W. Lo, J. E. Marsden, and S. D. Ross, *Dynamical Systems, the Three-Body Problem and Space Mission Design*. ISBN 978-0-615-24095-4: Marsden Books, 2022.
[15] V. Rom-Kedar and S. Wiggins, "Transport in two-dimensional maps," *Arch. Rat. Mech. Anal.*, Vol. 109, 1990, pp. 239–298.
[16] W. S. Koon, J. E. Marsden, S. D. Ross, M. W. Lo, and D. J. Scheeres, "Geometric mechanics and the dynamics of asteroid pairs," *Annals of the New York Academy of Sciences*, Vol. 1017, 2004, pp. 11–38.
[17] M. Dellnitz, O. Junge, W. S. Koon, F. Lekien, M. W. Lo, J. E. Marsden, K. Padberg, R. Preis, S. D. Ross, and B. Thiere, "Transport in dynamical astronomy and multibody problems," *Int. J. Bifurc. Chaos*, Vol. 15, 2005, pp. 699–727.

[18] S. D. Ross and P. Tallapragada, "Detecting and exploiting chaotic transport in mechanical systems," *Applications of Chaos and Nonlinear Dynamics in Science and Engineering* (S. Banerjee, L. Rondoni, and M. Mitra, eds.), Vol. 2, pp. 155–183, New York: Springer, 2012.
[19] M. A. Werner, *Multiple Gravity Assists for Low Energy Transport in the Planar Circular Restricted 3-Body Problem*. PhD thesis, Virginia Tech, 2022.
[20] D. J. Dichmann, R. Lebois, and J. P. Carrico, "Dynamics of Orbits Near 3:1 Resonance in the Earth-Moon System," *The Journal of the Astronautical Sciences*, Vol. 60, Mar 2013, pp. 51–86, 10.1007/s40295-014-0009-x.
[21] G. R. Ricker, J. N. Winn, R. Vanderspek, D. W. Latham, G. Á. Bakos, J. L. Bean, Z. K. Berta-Thompson, T. M. Brown, L. Buchhave, N. R. Butler, R. P. Butler, W. J. Chaplin, D. B. Charbonneau, J. Christensen-Dalsgaard, M. Clampin, D. Deming, J. P. Doty, N. D. Lee, C. Dressing, E. W. Dunham, M. Endl, F. Fressin, J. Ge, T. Henning, M. J. Holman, A. W. Howard, S. Ida, J. M. Jenkins, G. Jernigan, J. A. Johnson, L. Kaltenegger, N. Kawai, H. Kjeldsen, G. Laughlin, A. M. Levine, D. Lin, J. J. Lissauer, P. MacQueen, G. Marcy, P. R. McCullough, T. D. Morton, N. Narita, M. Paegert, E. Palle, F. Pepe, J. Pepper, A. Quirrenbach, S. A. Rinehart, D. Sasselov, B. Sato, S. Seager, A. Sozzetti, K. G. Stassun, P. Sullivan, A. Szentgyorgyi, G. Torres, S. Udry, and J. Villasenor, "Transiting Exoplanet Survey Satellite," *Journal of Astronomical Telescopes, Instruments, and Systems*, Vol. 1, No. 1, 2014, p. 014003, 10.1117/1.JATIS.1.1.014003.
[22] J. S. Parker and R. L. Anderson, *Low-Energy Lunar Trajectory Design*, Vol. 12 of *JPL Deep Space Communications and Navigation Series*. Hoboken, NJ: John Wiley & Sons, Inc., 1st ed., June 2014.
[23] K. C. Howell, D. C. Davis, and A. F. Haapala, "Application of Periapse Maps for the Design of Trajectories Near the Smaller Primary in Multi-Body Regimes," *Mathematical Problems in Engineering*, Vol. 2012, No. 1, 2012, p. 351759, https://doi.org/10.1155/2012/351759.
[24] B. Kumar, R. L. Anderson, and R. de la Llave, "High-order resonant orbit manifold expansions for mission design in the planar circular restricted 3-body problem," *Communications in Nonlinear Science and Numerical Simulation*, Vol. 97, 2021, p. 105691, https://doi.org/10.1016/j.cnsns.2021.105691.
[25] À. Haro, M. Canadell, J. Figueras, A. Luque, and J. Mondelo, *The Parameterization Method for Invariant Manifolds: From Rigorous Results to Effective Computations*, Vol. 195 of *Applied Mathematical Sciences*. Springer International Publishing, 2016.
[26] B. Kumar, R. L. Anderson, and R. de la Llave, "Rapid and accurate methods for computing whiskered tori and their manifolds in periodically perturbed planar circular restricted 3-body problems," *Celestial Mechanics and Dynamical Astronomy*, Vol. 134, No. 1, 2022, p. 3, 10.1007/s10569-021-10057-1.
[27] X. Wang and R. Malhotra, "Mean motion resonances at high eccentricities: The 2:1 and 3:2 interior resonances," *The Astronomical Journal*, Vol. 154, 2017, p. 20 (12 pp.).
[28] F. Namouni and M. H. M. Morais, "Resonance libration and width at arbitrary inclination," *Monthly Notices of the Royal Astronomical Society*, Vol. 493, 2020, pp. 2854—2871.
[29] L. Lan and R. Malhotra, "Neptune's resonances in the scattered disk," *Celestial Mechanics and Dynamical Astronomy*, Vol. 131, 2019, p. 39 (26pp).
[30] H. Poincaré, *Les Méthodes Nouvelles de la Mécanique Céleste (New Methods in Celestial Mechanics)*, Vol. 1-3. Paris: Gauthier-Villars, 1892-1899. Reprinted by Dover, New York, 1957.
[31] X. Wang and R. Malhotra, "Mean Motion Resonances at High Eccentricities: The 2:1 and the 3:2 Interior Resonances," *The Astronomical Journal*, Vol. 154, jun 2017, p. 20, 10.3847/1538-3881/aa762b.
[32] W. S. Koon, M. W. Lo, J. E. Marsden, and S. D. Ross, "Resonance and capture of Jupiter comets," *Celestial Mechanics and Dynamical Astronomy*, Vol. 81, 2001, pp. 27–38.
[33] S. D. Ross, "Trade-Off Between Fuel and Time Optimization," *New Trends in Astrodynamics and Applications*, College Park, MD, Jan. 2003, 2003.
[34] C. Jaffé, D. Farrelly, and T. Uzer, "Transition state in atomic physics," *Phys. Rev. A*, Vol. 60, 1999, pp. 3833–3850.
[35] E. M. Alessi, J. Masdemont, and A. Rossi, "The Earth-Moon System As a Dynamical Laboratory," *Frontiers in Astronomy and Space Sciences*, Vol. 6, 2019, 10.3389/fspas.2019.00043.